Research Square

Preprints are preliminary reports that have not undergone peer review.
They should not be considered conclusive, used to inform clinical practice,
or referenced by the media as validated information.

Sensory ultraviolet encoding by non-equilibrium trap dynamics in β-Ga2O3

Suin Yi

yisuin@tamu.edu

Texas A&M University https://orcid.org/0000-0001-7957-8953

Jae Young Kim

Byungsoo Kim

University of Virginia

Ho Won Jang

Seoul National University https://orcid.org/0000-0002-6952-7359

Suhas Kumar

Sandia National laboratories https://orcid.org/0000-0002-6772-7250

Article

Keywords:

Posted Date: November 12th, 2026

DOI: https://doi.org/10.21203/rs.3.rs-11218451/v1

License: This work is licensed under a Creative Commons Attribution 4.0 International License.
Read Full License

Additional Declarations: There is **NO** Competing Interest.

Sensory ultraviolet encoding by non-equilibrium trap dynamics in β-Ga_2O_3

Jae Young Kim[1†], Byungsoo Kim[2†], Ho Won Jang[3,4], Suhas Kumar[5,6*] and Su-in Yi[1*]*

[1]Department of Electrical and Computer Engineering, Texas A&M University, College Station, TX 77845, USA.
[2]Department of Electrical and Computer Engineering, University of Virginia, Charlottesville, VA 22904, USA.
[3]Department of Materials Science and Engineering, Research Institute of Advanced Materials, Seoul National University, Seoul 08826, Republic of Korea.
[4]Advanced Institute of Convergence Technology, Seoul National University, Suwon 16229, Republic of Korea.
[5]Nanyang Technological University, Singapore.
[6]Rain AI, San Francisco, CA 94403, USA.
[*]e-mail: yisuin@tamu.edu; su1@alumni.stanford.edu; hwjang@snu.ac.kr
†These authors contributed equally to this work.

Abstract

Deep-ultraviolet (DUV) sensing underlies safety-critical systems, especially flame and combustion detection, where detectors should both respond fast and reject false alarms from sources such as welding arcs. Conventional detectors offer no usable in-sensor dynamics, since trap-free devices offer a static response, while those laden with often-deep-level traps offer dynamics viewed as delaying a steady-state response. Thus, discriminating temporal features is deferred to downstream processing, forcing a trade-off between response time and accuracy. Here, in β-Ga_2O_3, we exploit such traps – DUV illumination photoactivates occupied traps, the Poole–Frenkel emission of which results in a current-controlled negative differential resistance (NDR). The NDR is out-of-equilibrium, existing only during photoactivation of traps away from a steady state. Coupled to a small external capacitance, this instability sustains voltage firing that is band-pass in effective dose rate. Reading the response at five different tuning currents distinguishes six DUV sources of identical wavelength, differing only in temporal modulation, including welding and flame that are indistinguishable by average intensity. This method offers 98.3% accuracy at 100 seconds versus 87.4% for an ideal intensity-only detector, thus discriminating dynamical information at the point of sensing versus by threshold-only. Therefore, defect dynamics treated as delaying the material's actual response, can encode useful information.

Introduction

Solar-blind detection of deep ultraviolet (DUV) light identifies the DUV signatures of failure in varied macro-scale applications such as power grid corona monitoring[1], flame detection in hydrogen infrastructure and industrial furnaces[2], and micro-scale applications such as on-chip (or in-package) discharge sensing in power electronics, especially those involving high-bandgap materials[3]. In such solar-blind DUV sensing, the emission of interest is detected by naturally filtering out much stronger visible and infrared background[4], but the detection process needs to carefully reject competing signals from other DUV sources, such as welding arcs[5]. β-Ga_2O_3 is among the most developed materials for DUV sensing[6,7], but its photoresponse is often governed by deep-level traps associated with oxygen vacancies and related defects[8], which capture and slowly re-emit photogenerated carriers. The resulting persistent photoconductivity extends the response over seconds to minutes[8]. This slow response is widely regarded as a major obstacle to practical devices, and much work has therefore been directed at suppressing its trap-related origins through growth control, annealing or heterostructure design[9–11].

Suppressing trap-limited response improves the response speed of photodetection, and enables a clean and near-instantaneous tracking of the temporal changes in the source. However, such a faithful temporal tracking also means that the sensing medium lacks any discrimination of its own. As such, the source identity must be inferred by post-processing the resulting electrical waveform, thereby needing a two-stage process. For example, in DUV monitoring, welding arcs, lightning and corona are common false-alarm sources for ultraviolet flame detectors that do not carefully discriminate temporal patterns in the source (e.g., in threshold-type detectors)[12,13]. Such false signals need to be rejected not by their intensity but by their spectral or temporal cues, such as flickering[14]. Commercial flame-detection systems address this ambiguity using post-sensing spectral channels[12] or alarm-verification procedures[15]. More recently, machine-learning approaches have extracted discriminating features from recorded photocurrent waveforms[16]. No matter the sophistication of such approaches, post-processing introduces a delay in the response time. Discriminating temporal features of the inputs through the intrinsic dynamics of the detecting medium itself would allow temporal discrimination to arise in the sensor response[17–21] rather than in downstream signal processing. Discriminating temporal features have not, however, been shown to arise from the intrinsic transport dynamics of a single photodetector (since such dynamics have thus far been viewed as parasitic[8–11]).

Here we examine β-Ga_2O_3 phototransistors in which the same deep levels that are considered to slow the photoresponse can, under illumination, render the device locally active [22–24] (i.e., capable of self-dynamics owing to instabilities). Instead of suppressing the slow relaxation of trap occupancy, we engineered the material (and the device structure) to exhibit varying dynamical responses that are sensitive to the temporal structure of illumination. Under DUV illumination, Poole–Frenkel emission from occupied traps lowers the effective transport barrier[25,26] and drives a current-controlled negative

differential resistance (NDR)[27] that is absent in the dark (Fig. 1a, c–f). Current-controlled instabilities in oxide devices are often driven by Joule heating[28–30], with temperature as the state variable. Our measurements, based on temperature and sweep rate, together with a trapping–emission model, instead indicate non-equilibrium trap occupancy as the internal state governing the instability, meaning that the internal state is directly coupled to the DUV illumination being sensed. Coupling the device to a small external capacitance produces self-sustained voltage firing[31,32], the DC level of which is monotonic and the AC amplitude of which is band-pass in the effective dose rate, with both responses tunable by the bias current (Fig. 1b, g, h), thereby offering multiple degrees of tunability in sensing. Reading these responses at multiple tuning currents distinguishes six DUV inputs sharing a single wavelength and differing only in temporal modulation (Fig. 1i).

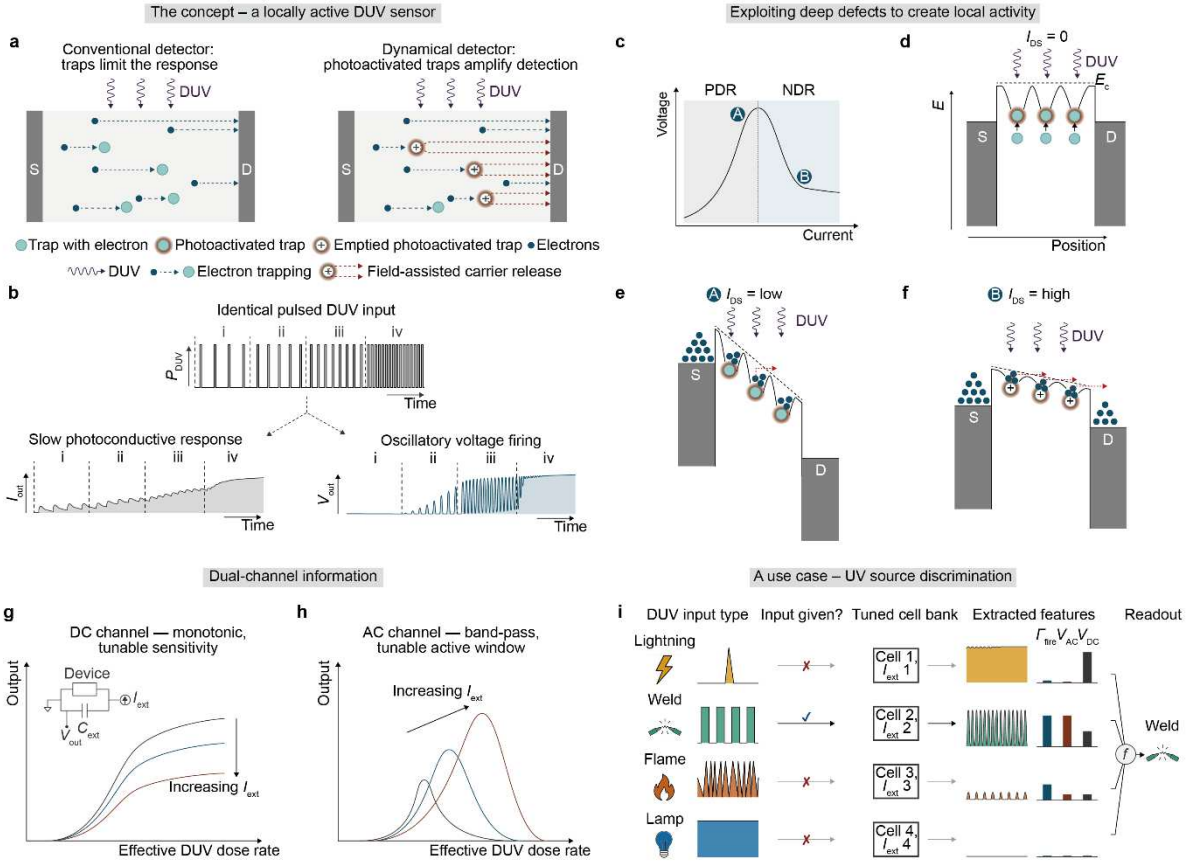


Figure 1 | Defect-enabled dynamical DUV sensing. a, Operating principle of a conventional detector, in which trap states limit the response, and of a dynamical detector, in which photoactivated traps confer local activity. **b,** Responses of the two detectors to pulsed deep-ultraviolet (DUV) inputs of fixed irradiance and pulse width, with duty cycle increasing from i to iv. Photocurrent under voltage bias is measured in the conventional detector, while a voltage under current drive is read out in the dynamical detector (in the response/firing curves, the corresponding effective dose rate increases from i to iv). The conventional response is slow and saturating. The dynamical response shows no firing in (i), weak firing in (ii), sustained firing in (iii) and suppression in (iv). **c,** Current-sourced drain–source voltage (V_{DS})–current (I_{DS}) characteristic. Ⓐ and Ⓑ mark operating points on the positive-differential-resistance (PDR) and negative-differential-resistance (NDR) branches. **d,** Band diagram at $I_{DS} = 0$. E_c, conduction-band edge. **e, f,** Band diagrams at Ⓐ (low I_{DS}, high V_{DS}) and at Ⓑ (high I_{DS}, low V_{DS}). Ⓑ shows greater Poole–Frenkel emission and a lower barrier. Red dashed arrows indicate Poole–Frenkel emission. **g,** DC channel, increasing monotonically with the effective DUV dose rate. Increasing tuning current I_{ext} shifts the response downwards. Inset, operating circuit, in which the device is driven at constant I_{ext} in parallel with an external capacitance C_{ext} = 10 pF and the output signal V_{out} is read from the operating circuit. **h,** AC channel, band-pass in the effective DUV dose rate. Increasing I_{ext} shifts the pass-

band to higher dose rate. **i,** Conceptual scheme for discriminating DUV sources. Sources differing in temporal structure drive a bank of cells tuned by different I_{ext}, one source at a time. Each source produces a distinct combination of extracted metrics across the bank; three metrics are shown here. A readout identifies the source. All panels are illustrations and contain no measured data.

Results

NDR and its mechanism

We fabricated β-Ga_2O_3 phototransistors on sapphire, in which a Ni/Au top electrode overlies an Al_2O_3 dielectric and Ti/Au source and drain electrodes contact the channel (Fig. 2a, also see Methods). Using cross-sectional transmission electron microscopy, we confirmed epitaxial registration with the substrate and a clean film–substrate interface (Fig. 2b). The room-temperature photoluminescence spectrum indicates two defect-related bands in the as-grown films (Fig. 2c), assigned to a dominant oxygen-vacancy-related donor–acceptor recombination and a weaker emission from other defect states (at much deeper levels)[33–35].

Sweeping the current at a compliance of 40 V, we observed a region of current-controlled NDR under DUV illumination (Fig. 2d), whereas the dark response remained compliance-limited over the same current range. NDR in β-Ga_2O_3 has previously been reported under voltage sweep[36], where it has been attributed to oxygen-vacancy migration and occurs in the dark; here, by contrast, the instability (NDR) appears only under illumination and is resolved under current sweep as a single-valued curve that is a function of the applied current.

To determine how illumination modifies the transport barrier, we measured the drain current (I_{DS}) over the temperature range 296–345 K at a fixed drain–source voltage (V_{DS}), and obtained the effective activation energies via Arrhenius fits at each V_{DS} (Fig. 2e). The activation energy decreases from about 1.10 eV in the dark to about 0.36 eV under DUV at high bias. By calculating the local slopes of the current-voltage curves, we confirmed that a Poole–Frenkel-type emission was activated along with barrier lowering[26,37] (Supplementary Section 1). These observations indicate that DUV illumination increases trap energies, allowing them to trap carriers, thereby building up a transport barrier[38] (that is, with increasing I_{DS}, as traps fill, V_{DS} rises up to a certain threshold). At sufficiently high V_{DS}, field-driven emission overtakes trap filling, leading to a runaway effect involving a drop in V_{DS} and emptying of traps reinforcing each other (that is, as I_{DS} increases beyond a threshold, with the corresponding V_{DS} exceeding a threshold, there is a drop in V_{DS}). This rise-and-fall process results in NDR. A quantitative model of this process agrees with experimental data (Supplementary Section 1).

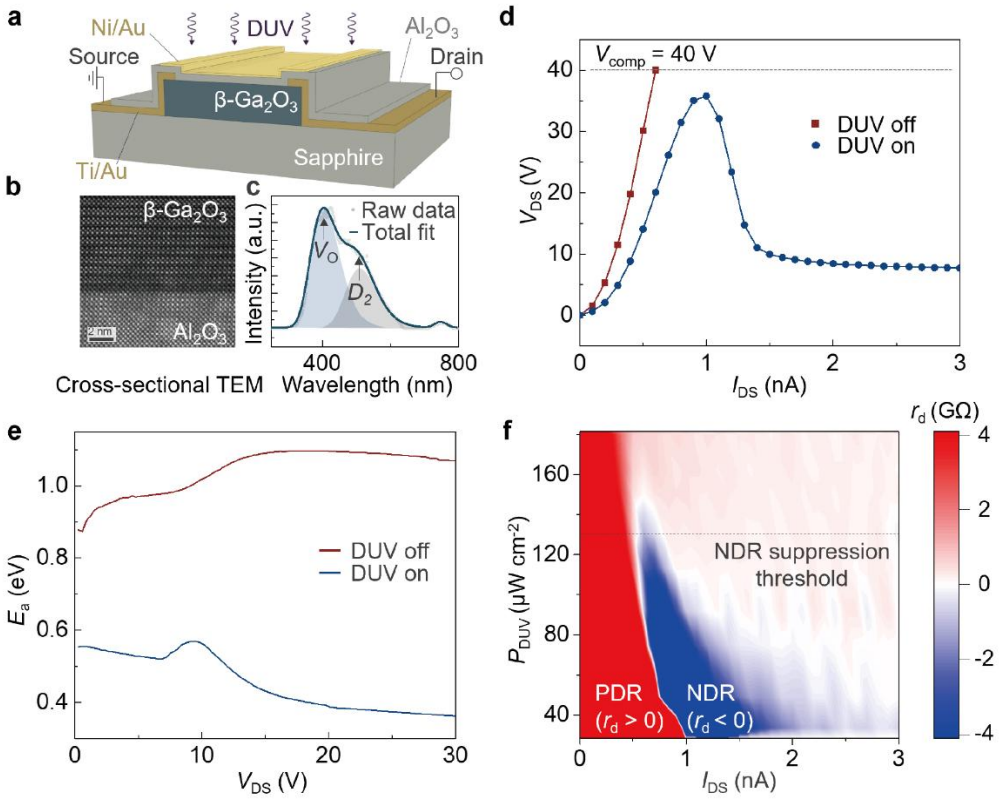


Figure 2 | β-Ga_2O_3 phototransistor and its DUV-activated NDR. a, Device schematic. A β-Ga_2O_3 channel carries a Ni/Au top electrode over an Al_2O_3 dielectric, with Ti/Au source and drain electrodes on a sapphire substrate. **b,** Cross-sectional transmission electron micrograph of the film on the substrate. Scale bar, 2 nm. **c,** Room-temperature photoluminescence spectrum with its total fit. V_O band is assigned to oxygen-vacancy-related donor–acceptor recombination; D_2 indicates emission from other defect states. **d,** Current-controlled output characteristics under DUV-off and DUV-on at DUV irradiance P_{DUV} = 34 μW cm^{-2}. Under DUV, an NDR emerges below the 40 V compliance (V_{comp}), whereas the dark response remains compliance-limited. **e,** Effective activation energy (E_a) versus V_{DS} in the dark and under DUV at P_{DUV} = 11 μW cm^{-2}. **f,** Differential resistance (r_d) as a function of I_{DS} and P_{DUV}, separating the positive-differential-resistance (PDR, $r_d > 0$) and negative-differential-resistance (NDR, $r_d < 0$) regions. The map is interpolated for display from a 31 × 12 measured grid. Dashed horizontal line indicates the NDR suppression threshold at about 130 μW cm^{-2}. Color scale is clipped at ±4 GΩ.

We mapped the differential resistance r_d against the applied current and DUV irradiance (Fig. 2f). The NDR region ($r_d < 0$, blue) is bounded within a range on both axes: it opens above a current threshold that decreases with irradiation and closes entirely above an irradiance of about 130 μW cm^{-2}. Consistent with the competition between trap filling and field emission inferred from the model, NDR intensity monotonically decreases with irradiance and eventually vanishes. Under these fast-sweep conditions the device is therefore locally active only within a finite current–irradiance window.

The NDR as a non-equilibrium process

We next sought to establish the kinetics of the NDR. Current-controlled NDR in oxide devices is commonly driven by Joule heating[28–30], in which superlinear thermally activated transport provides positive feedback and the device temperature acts as the state variable. In such an electrothermal picture, increasing the ambient temperature shifts the electrical conditions required to access the instability (NDR). Here, however, the NDR window narrows progressively between 296 and 303 K (Fig. 3a), while

both the peak-to-valley voltage difference and the minimum differential resistance approach zero (Fig. 3b,c), leaving an entirely positive-differential response above about 302 K. This behavior is difficult to reconcile with a simple Joule-heating-driven instability and instead suggests that temperature modifies the non-equilibrium state required for NDR.

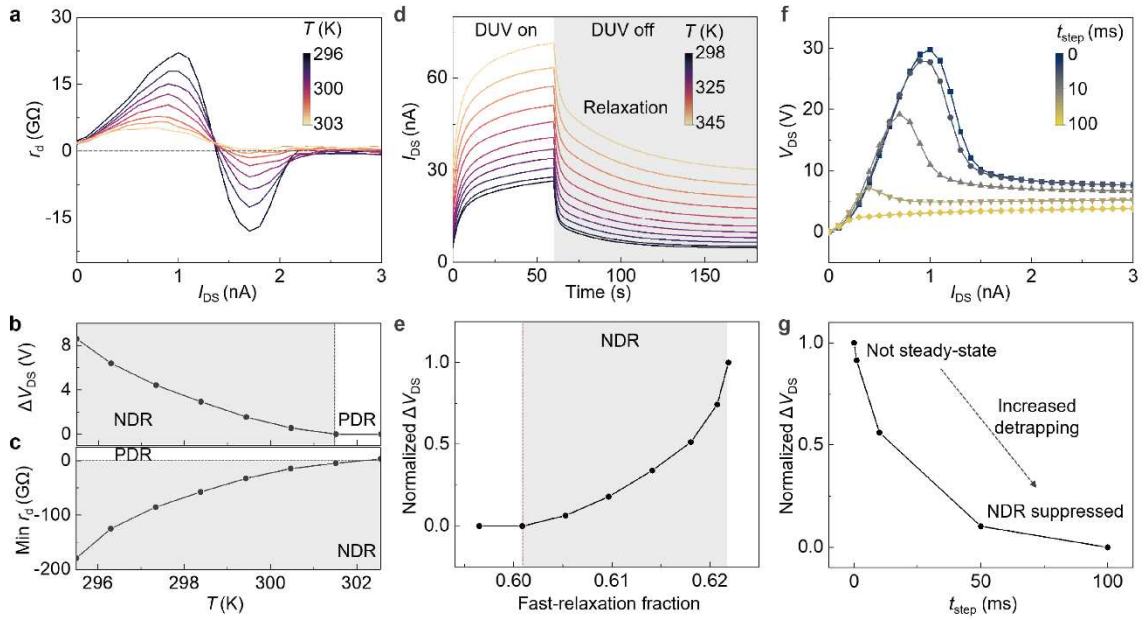


Figure 3 | Thermal and sweep-rate control of trap-mediated NDR. a, r_d as a function of I_{DS} under DUV illumination (P_{DUV} = 11 μW cm^{-2}) at ambient temperatures from 296 to 303 K. **b, c,** Peak-to-valley voltage difference (ΔV_{DS}) and minimum differential resistance (min r_d) versus temperature. Shading marks the NDR region. **d,** Time-resolved I_{DS} at V_{DS} = 10 V during and after DUV illumination (P_{DUV} = 11 μW cm^{-2}) at ambient temperatures from 298 to 345 K. Shading marks the post-illumination relaxation window. **e,** Normalized ΔV_{DS} versus the fast-relaxation fraction $A_1/(A_1 + A_2)$. A_1 and A_2, amplitudes of the fast (τ_1) and slow (τ_2) relaxation components. Dashed vertical line indicates onset of the NDR response at a fast-relaxation fraction of about 0.60. **f,** V_{DS} versus I_{DS} under DUV (P_{DUV} = 34 μW cm^{-2}) at sweep step times t_{step} from 0 to 100 ms. **g,** Normalized ΔV_{DS} versus t_{step}, showing the progressive suppression of NDR as more time is allowed for relaxation.

To characterize the associated relaxation kinetics, we recorded I_{DS} during and after DUV illumination between 298 and 345 K (Fig. 3d). We fit the post-illumination decay using two exponential components, a fast and a slow one, with each of their time constants increasing with temperature (Supplementary Section 2). We then plotted the peak-to-valley voltage difference against the fraction of the amplitude of the fast relaxation exponent $A_1/(A_1 + A_2)$, where A_1 and A_2 are the amplitudes of the fast and slow relaxation exponents, respectively (Fig. 3e). The NDR magnitude correlates with the redistribution between the two relaxation components, with the onset of NDR coinciding with a fast-relaxation fraction of about 0.60. Because both quantities vary with temperature, however, this correlation alone does not establish whether relaxation rather than temperature controls the instability.

We therefore varied the measurement timescale at fixed temperature and illumination, thereby changing the time available for detrapping without altering the external conditions. Increasing the sweep's step time from 0 to 100 ms progressively suppressed the peak-to-valley height (Fig. 3f,g), as more time was allowed for trap relaxation during the sweep. Because this suppression is obtained at fixed temperature, it independently supports incomplete trap relaxation as a requirement for NDR. The

suppression at longer step times also argues against an instability dominated by progressive mobile-ion redistribution, which longer times would be expected to favour[36]. Together with the field-assisted barrier lowering and trapping-emission model inferred from Fig. 2, and the temperature-dependent relaxation of Fig. 3d,e, these results support the non-equilibrium occupancy of photoactivated traps as the internal state governing the instability.

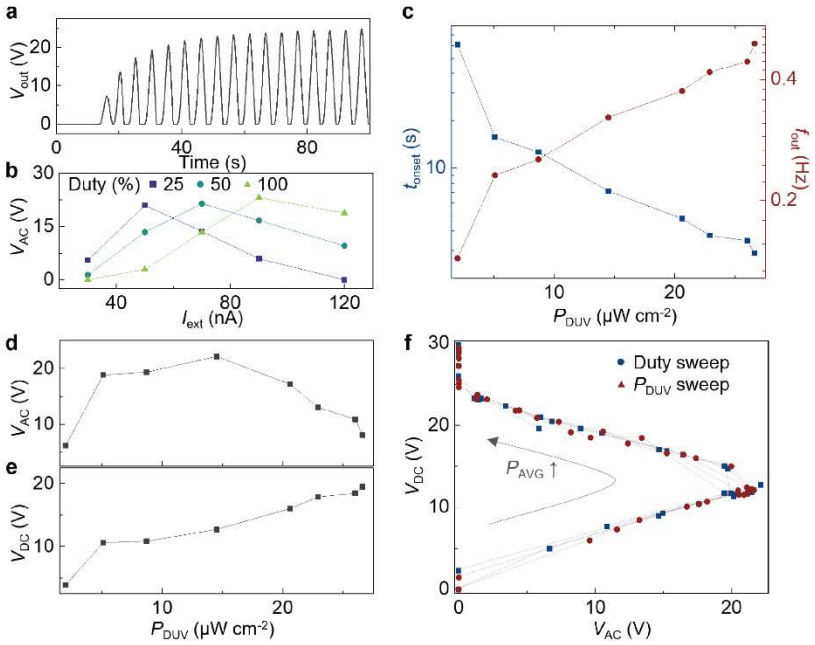


Figure 4 | Current-tuned band-pass firing and dual-channel encoding. a, Representative oscillatory response (V_{out} versus time) at I_{ext} = 70 nA, P_{DUV} = 5 μW cm^{-2} and duty = 50%. **b,** AC amplitude V_{AC} versus I_{ext} at duty cycles of 25, 50 and 100% (P_{DUV} = 5 μW cm^{-2}). The peak shifts to higher I_{ext} at higher duty cycle. **c,** Firing-onset time (t_{onset}, left axis) and output frequency (f_{out}, right axis) versus P_{DUV} at I_{ext} = 120 nA and duty = 100%. At this duty cycle, P_{DUV} equals the effective dose rate P_{AVG} (= P_{DUV} × duty). Vertical axes are logarithmic. **d, e,** V_{AC} and DC level V_{DC} versus P_{DUV} under the conditions of **c**. **f,** V_{DC} versus V_{AC} under a duty-cycle sweep (P_{DUV} = 15 μW cm^{-2}) and a P_{DUV} sweep (duty = 50%), with I_{ext} from 30 to 120 nA. Arrow marks the direction of increasing P_{AVG}.

A true test of local activity (arising from current-controlled NDR) is the ability of a device to produce self-oscillations when destabilized by a parallel capacitor and driven by a current source (Fig. 1g, inset)[31,32]. Such local activity would confirm internal kinetics of the device. To verify the presence of local activity, we placed the device in parallel with an external capacitance C_{ext} of 10 pF and recorded the resulting output voltage. Under pulsed DUV illumination, the output voltage rises and begins to oscillate (fire)[39] after a delay, developing into sustained firing, the amplitude of which evolves over tens of seconds (Fig. 4a). Firing occurs only within a window of the tuning current I_{ext}, and the window shifts to higher I_{ext} as the duty cycle of the input is raised (Fig. 4b), so both the optical input and the electrical bias set whether the device fires. Unlike the fast current sweeps used to map the NDR boundary in Fig. 2f, the measurements in Fig. 4 operate the device–capacitor circuit at a fixed external tuning current over the full observation window.

Since the input is temporally varying, it is reasonable to check whether temporally varying dynamics

in the output merely reflect the dynamics of the input – in such a case, the detector would not be discriminating among different inputs. With separate experiments, we confirmed that the output frequency stayed constant even when the input frequency was varied within a certain frequency range, and the system produced firing of the output even when the input was constant irradiation (with no dynamics), detailed in Supplementary Section 3. Thus, the input-dependent dynamics characterized here are true measures of the sensing medium's discriminating kinetic response to the inputs.

These results indicate that the NDR is a kinetic, non-equilibrium response that persists only while the trap occupancy remains displaced from its steady-state value.

Encoding DUV dynamics in multiple independent variables

The richness of a dynamical response is often determined by the number of nominally independent variables that can be mapped onto the dynamics [31,40–42], which leads to encoding a high density of information, which in turn enables a better detector. Here we identified five such measurable variables.

Varying the DUV irradiance P_{DUV} at fixed duty cycle, the firing-onset time decreases and the output frequency increases monotonically with P_{DUV} (Fig. 4c). In contrast, the AC amplitude passes through a maximum at 15 μW cm^{-2} before declining, whereas the DC level increases monotonically (Fig. 4d,e). The AC channel is therefore band-pass in the optical drive, whereas the DC channel is monotonic (as illustrated in Fig. 1g,h). Sweeping the duty cycle at fixed irradiance and sweeping the irradiance at fixed duty cycle, both collapse onto a common trajectory in the plane plotting DC level against AC amplitude (Fig. 4f). This result indicates that under periodic drive at fixed pulse width, the operating point is governed by the effective dose rate $P_{AVG} = P_{DUV} \times$ duty, rather than by irradiance or duty cycle independently (additional plots in Supplementary Figs. S6–S8). These observations identify two distinct encoding variables: V_{AC}, which is band-pass, and V_{DC}, which is monotonic (both with respect to P_{DUV}).

The firing-onset time, t_{onset}, follows a power-law dependence on effective dose rate, which shifts systematically with I_{ext} (Supplementary Fig. S9b). We also identified the output frequency, f_{out}, and the firing rate, Γ_{fire}, as two other independent variables – f_{out} identifies the most dominant spectral frequency, while Γ_{fire} measures the number of fired spikes within a time window. As such, a steady fast flicker, as in a flame, could have a high f_{out} and a high Γ_{fire}, whereas intermittent bursts, as in a welding arc, could have an equally high f_{out} but a lower Γ_{fire} (Supplementary Section 3). As a result, we have five variables to encode the input dynamics: V_{AC}, V_{DC}, t_{onset}, f_{out}, and Γ_{fire}.

Source discrimination by current-tuned firing

To test whether the five metrics carry source identity, we mimicked an array of five detectors, each biased at a different tuning current (I_{ext}). As a result, we obtained a 25-element fingerprint for each measurement (Fig. 5a). We used six DUV inputs derived from a single 265 nm source (that is, the same amplitude and wavelength), differing only in how the illumination is distributed in time (Fig. 5b). The

set comprises a continuous lamp, a weld waveform and an irregular flame with the same duty cycle but different temporal structures, a second block-structured weld waveform, a sparse corona and a single lightning flash. Because all six share the same wavelength, spectral information alone cannot distinguish them; because several also share the same duty cycle, time-averaged irradiance alone cannot fully separate the six inputs. Weld 1 and flame were designed to have the same nominal effective dose rate but distribute their pulses differently in time. When burst intervals become comparable to the trap-relaxation timescale, the trap state can retain sensitivity to pulse ordering, so inputs with similar P_{AVG} need not follow the same dynamical trajectory. The five tuning-current responses were measured sequentially on one device and then combined to mimic the output of an array of cells operating in parallel.

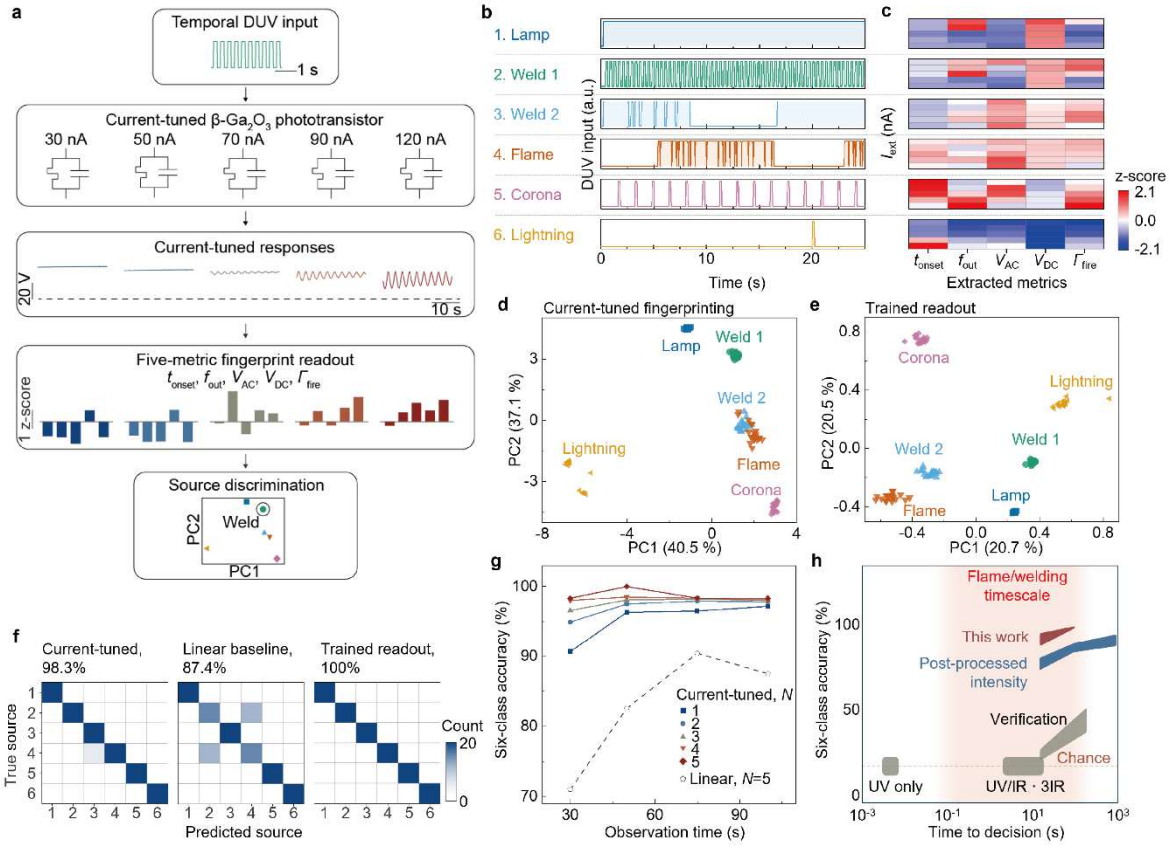


Figure 5 | Source discrimination by current-tuned firing. a, Signal-processing pipeline, illustrated with a measured trace from the weld 1 input. A temporal DUV input drives the phototransistor at five tuning currents I_{ext} (30, 50, 70, 90 and 120 nA). Five metrics — t_{onset}, f_{out}, V_{AC}, V_{DC} and Γ_{fire} — are extracted and passed to a readout that identifies the source. **b,** DUV input waveforms representing the six sources, numbered 1–6 and differing in temporal structure at fixed peak irradiance. **c,** Fingerprints of the five metrics across the five tuning currents for each source, shown as *z*-scores. I_{ext} increases from 30 nA at the bottom to 120 nA at the top. **d,** Principal-component projection of the standardized fingerprints. **e,** Principal-component projection of the ridge score vectors obtained from the fingerprints in **c**. **f,** Confusion matrices at an observation time t_{obs} = 100 s for the nearest-centroid readout using five tuning currents, the ideal linear baseline reporting time-averaged irradiance, and the trained ridge readout, using the source numbering of **b**. Each source was measured over 20 trials. **g,** Six-class accuracy versus observation time for nearest-centroid readouts using N = 1–5 tuning currents and for the ideal linear baseline. **h,** Six-class accuracy versus time to decision for the current-tuned readout and for the ideal linear baseline followed by post-processing, together with representative response-time ranges of commercial flame detectors and alarm-verification windows. The device region spans N = 1–5 tuning currents; the post-processed region spans N = 1–5 ideal linear baselines and nearest-centroid to multilayer-perceptron readouts, projected beyond 100 s by scaling the readout noise with observation time. The vertical

placement of the commercial-detector and verification regions is schematic. Shading indicates characteristic flame and welding timescales.

The fingerprints show source-dependent patterns across the six inputs (Fig. 5c). In the first two principal components, most sources form separated clusters, although flame and weld 2 partly overlap (Fig. 5d). A nearest-centroid readout applied to the standardized fingerprints identifies the source with 98.3% accuracy at an observation time t_{obs} of 100 s, compared with 87.4% for an ideal linear baseline (the output of which is proportional to the time-averaged irradiance of the same drive waveform) (Fig. 5f). The residual error is confined to flame and weld 2, the pair that overlaps in Fig. 5d. Adding a trained linear classifier that takes the 25-element fingerprint can clearly separate flame and weld 2 in the score space (Fig. 5e), and reaches 100% classification accuracy (Fig. 5f). We use the nearest-centroid readout as the primary comparison because its low-capacity, prototype-based decision rule provides a simple test of the separability already present in the device-derived feature space.

The ideal linear baseline includes Gaussian readout noise but no response-time or saturation limit (Supplementary Section 4). Even under these idealized conditions, time-averaged intensity does not fully separate weld 1 from flame because they were designed to deliver the same time-averaged irradiance while differing only in temporal arrangement. By contrast, V_{DC} at a single tuning current provides greater separation between the two classes. Classification accuracy of the device-derived fingerprints increases with observation time and with the number of tuning currents, and remains above the linear baseline over the measured observation window (Fig. 5g). The baseline accuracy reaches a minimum near t_{obs} = 30 s, where the cumulative duty cycle of weld 2 crosses those of weld 1 and flame, causing the three inputs to transiently overlap in time-averaged intensity. To test whether the remaining baseline error arose from readout noise or classifier choice, we repeated the linear-baseline analysis in the noise-free limit using nearest-centroid, ridge, multilayer-perceptron and quadratic support-vector readouts. All four reach at or below 95.0% accuracy and misclassify weld 1 trials as flame. This common error pattern indicates that the residual limit arises from the information retained in time-averaged intensity rather than from readout noise or classifier choice.

Placing these results against existing approaches requires care, because accuracy and decision time are reported for different tasks. Commercial DUV flame detectors respond within seconds but issue an alarm rather than a source identity, so no six-class accuracy is defined for them (Fig. 5h). Most reported ultraviolet source-classification systems distinguish physically distinct emitters and construct discriminating features through downstream processing, making their reported accuracies not directly comparable with the single-wavelength temporal-discrimination task studied here (Supplementary Table 3). We therefore show in Fig. 5h the region occupied by the device readout together with that of the ideal linear baseline followed by post-processing. The commercial groups are shown schematically at the six-class chance level only to indicate that source identity is not among their outputs, not as a measured classification accuracy. The shaded band provides context for the characteristic timescales over which

flame and welding signals evolve. With multiple tuning currents, the device readout reaches accuracies beyond the 95.0% limit of the linear route. The resulting decision time is of order tens of seconds, reflecting the slow trap-relaxation dynamics that generate the firing rather than the response time of a threshold detector. This timescale overlaps the characteristic flame and welding timescales shown for context in Fig. 5h. The comparison therefore separates two effects: the trap dynamics set the decision time, and they also generate discriminating information that time-averaged intensity does not retain.

Conclusion

We explored the broad question on whether defect-rich wide-bandgap semiconductors can be a design principle, rather than being the subject of costly engineering efforts to remove such defects or avoid their effects. Especially deep-level defects are conventionally treated as parasitics, since they slow the photoresponse in wide-bandgap materials. Here, operating the device away from equilibrium makes the kinetics of photoactivated traps a functional degree of freedom. Specifically, the non-equilibrium occupancy of photoactivated traps, in competition with field-induced Poole–Frenkel emission (emptying of traps), becomes a state variable that enables DUV-activated current-controlled NDR in β-Ga_2O_3. As such, instead of the traditional thermally activated NDR, we have isolated an optically-driven NDR. We show that the NDR is a fingerprint of underlying local activity, which is the medium's unique kinetic behavior that produces self-sustained oscillations when placed in parallel with a capacitor. Further, we identify five measurable variables, each of which offers distinct identifications of the input's dynamics. Thus, even when the input sources were identical in wavelength and amplitude, differing only in their temporal distribution, we were able to discriminate between industrially relevant DUV signatures, such as those representing welding, flames, arcs, etc. Therefore, defect dynamics that ordinarily limit photodetection can become a source of function when they are deliberately incorporated into the device dynamics.

Methods

Film growth and device fabrication

β-Ga_2O_3 films were grown on c-plane sapphire by pulsed laser deposition using a KrF excimer laser at 248 nm. The fluence was 2.5 J cm^{-2}, the repetition rate 2 Hz, the substrate temperature 650 °C, the oxygen pressure 1 mTorr and the target–substrate distance 50 mm, giving a film thickness of about 300 nm. Devices were patterned by maskless lithography and inductively coupled plasma etching, with a channel of 80 μm × 20 μm. Ti/Au (50/100 nm) source and drain electrodes were deposited by electron-beam evaporation, followed by 110 nm of Al_2O_3 by thermal atomic layer deposition at 250 °C using trimethylaluminium, and Ni/Au (10/10 nm) top electrodes by electron-beam evaporation. The 24 × 24 array was fabricated by the same process on a single chip; all electrical measurements reported here were made by contacting individual phototransistors through their source and drain electrodes. The

firing characteristics were additionally measured on four cells from the same array (Supplementary Section 5).

Structural and optical characterization

X-ray diffraction was performed on a PANalytical X'Pert Pro diffractometer using Cu Kα radiation (λ = 1.54056 Å). θ–2θ scans were collected over 10°–110° at room temperature, and ϕ scans of the β-Ga_2O_3 ($4\bar{0}1$) and Al_2O_3 (116) reflections were used to assess in-plane epitaxial registry. Cross-sectional specimens were imaged on a JEOL JEM-2100F. Room-temperature photoluminescence was measured on a PicoQuant FluoTime 300 spectrometer at an excitation wavelength of 266 nm and deconvoluted in wavelength space into three Gaussian components centred at 405, 511 and 749 nm. The assignments of the two dominant components are consistent with reported spectral positions; the corresponding optical transition energies are distinct from the effective activation energies of Fig. 2e.

Electrical measurements

All electrical measurements were performed in ambient atmosphere using a Keysight B1500A semiconductor parameter analyser, with the device driven by a high-power source-measure unit at a voltage compliance of 40 V and the drain connected to the ground unit. Current-driven drain–source voltage (V_{DS})–current (I_{DS}) sweeps were performed up to 3 nA with no intentional delay between successive steps unless stated. The oscillation measurements were instead performed at a fixed tuning current held over the full observation window. For the sweep-rate measurements, the programmed step time was varied from 0 to 100 ms. Temperature-dependent transport and post-illumination relaxation measurements were performed between 296 and 345 K. The specific irradiance, bias and temperature conditions for each dataset are given in the corresponding figure captions.

For the irradiance-dependent measurements of Fig. 2f and Supplementary Fig. S4, P_{DUV} was varied from 29 to 180 μW cm^{-2}. The differential resistance r_d of Fig. 2f was obtained by numerical differentiation on a 31 × 12 measured grid of I_{DS} and P_{DUV} and interpolated for display. The differentiation noise floor was 0.54 GΩ, propagated from the repeat-to-repeat spread of V_{DS}; a negative excursion was classified as NDR only where r_d fell below three times this floor.

DUV illumination

Illumination was provided by a 265 nm light-emitting diode (M265L5) gated by a medium-power source-measure unit of the same analyser at a drive voltage of 5 V. The optical irradiance at the device plane was calibrated using an S120VC sensor and a PM100D2 console. For the parameter-grid measurements, the pulse width was held fixed at 200 ms, so duty cycles of 12.5, 25, 40, 50, 66.7 and 80% correspond to input repetition rates f_{in} of 0.625, 1.25, 2.0, 2.5, 3.33 and 4.0 Hz, respectively. A duty cycle of 100% denotes continuous illumination, for which f_{in} is not defined.

Oscillation measurements and metric extraction

An external capacitance of 10 pF was connected in parallel with the device, and the voltage at the common node was recorded at approximately 62 Hz. The tuning current I_{ext} was supplied to the parallel device–capacitor network and is distinct from the instantaneous device current I_{DS}. For the oscillation measurements, the reported output voltage was defined as $V_{out} = V_{comp} - V_{DS}$, with V_{comp} = 40 V, and tuning currents I_{ext} of 30, 50, 70, 90 and 120 nA were applied. The five tuning currents were applied sequentially to a single device; the parallel-bank configuration in Fig. 1i represents the corresponding operating concept. Five metrics — the firing-onset time t_{onset}, output frequency f_{out}, AC amplitude V_{AC}, DC level V_{DC} and firing rate Γ_{fire} — were extracted from each response. Their definitions, signal-processing procedures and response-map construction are given in Supplementary Section 3. Conditions in which the output frequency locked to the input pulse rate were excluded from the output-frequency analysis in the parameter grid; no such exclusion was applied in the source-discrimination measurements, where an input-locked response is itself a signature of the source.

Source discrimination

Six temporal drive waveforms representing a continuous lamp, two welding conditions, flame, corona and lightning were generated from the same 265 nm source, such that the task contained no spectral information and class differences arose only from temporal modulation. Each input was measured over 20 trials. For each trial, the five metrics extracted at each of the five tuning currents were concatenated to form a 25-element fingerprint. Source classification was evaluated by leave-one-trial-out cross-validation using a nearest-centroid readout, with ridge regression used as a trained comparison. The linear baseline was constructed from the time-averaged irradiance of the same drive waveform with Gaussian readout noise but no response-time or saturation limit. Full waveform parameters, metric handling, classification procedures and baseline construction are given in Supplementary Section 4.

Data Availability

The datasets generated and/or analysed during the current study are available from the corresponding author upon reasonable request.

Code Availability

The custom Python code used for the model fitting, metric extraction and classification analyses is available from the corresponding author upon reasonable request and will be deposited in a public repository upon publication.

Acknowledgements

This research was supported by Young Investigator Program (YIP) from Air Force Office of Scientific Research (grant no. AFOSR-FA9550-25-1-0099).

Author Contributions

J.Y.K. and B.K. contributed equally to this work. J.Y.K. and B.K. jointly designed and fabricated the β-Ga_2O_3 phototransistors. J.Y.K. performed the measurements, analysed the data and wrote the manuscript. H.W.J. provided guidance on film growth and device fabrication. S.K. conceived the dynamical-sensing framing and guided the interpretation of the NDR dynamics. S.Y. conceived and supervised the project. All authors discussed the results, contributed to manuscript revision and approved the final manuscript.

Competing Interests

The authors declare no competing interests.

References

1. Pinnangudi, B., Gorur, R. S. & Kroese, A. J. Quantification of corona discharges on nonceramic insulators. IEEE Trans. Dielectr. Electr. Insul. 12, 513–523 (2005).
2. Arens, E. E., Youngquist, R. C. & Starr, S. O. Intensity calibrated hydrogen flame spectrum. Int. J. Hydrogen Energy 39, 9545–9551 (2014).
3. Wang, L. et al. A review of partial discharge in medium voltage SiC power modules under square wave excitation: characterization, mitigation, and detection. IEEE J. Emerg. Sel. Top. Power Electron. 12, 3588–3606 (2024).
4. Chen, X., Ren, F., Gu, S. & Ye, J. Review of gallium-oxide-based solar-blind ultraviolet photodetectors. Photonics Res. 7, 381–415 (2019).
5. Razeghi, M. & Rogalski, A. Semiconductor ultraviolet detectors. J. Appl. Phys. 79, 7433–7473 (1996).
6. Pearton, S. J. et al. A review of Ga2O3 materials, processing, and devices. Appl. Phys. Rev. 5, 011301 (2018).
7. Higashiwaki, M., Sasaki, K., Kuramata, A., Masui, T. & Yamakoshi, S. Gallium oxide (Ga2O3) metal-semiconductor field-effect transistors on single-crystal β-Ga2O3 (010) substrates. Appl. Phys. Lett. 100, 013504 (2012).
8. Tak, B. R., Yang, M. M., Alexe, M. & Singh, R. Deep-level traps responsible for persistent photocurrent in pulsed-laser-deposited β-Ga2O3 thin films. Crystals 11, 1046 (2021).
9. Langpoklakpam, C. et al. State-of-the-art solar blind and X-ray photodetectors based on gallium oxide. Adv. Photonics Res. 6, 2500008 (2025).
10. Wang, J. et al. Regulation of oxygen vacancies in nitrogen-doped Ga2O3 films for high-performance MSM solar-blind UV photodetectors. J. Mater. Chem. C 11, 6202–6211 (2023).
11. Wang, H. et al. High-sensitivity and fast-response solar-blind photodetectors via band offset engineering for motion tracking. Nat. Commun. 16, 1234 (2025).
12. Liu, Z. & Kim, A. K. Review of recent developments in fire detection technologies. J. Fire Prot. Eng. 13, 129–151 (2003).
13. Castleman, W. L., Selstad, J. T. & Lapp, D. F. Process and system for flame detection. US patent 6,046,452 (2000).
14. Traina, J. E. Ultraviolet radiation detector. US patent 4,016,424 (1977).
15. National Fire Protection Association. NFPA 72, National Fire Alarm and Signaling Code (NFPA, Quincy, MA, 2025).
16. Park, T. et al. An integrated wireless deep-UV sensing system for intelligent early fire detection. Sci. Adv. 12, eaef4143 (2026).
17. Mennel, L. et al. Ultrafast machine vision with 2D material neural network image sensors. Nature 579, 62–66 (2020).
18. Zhou, F. & Chai, Y. Near-sensor and in-sensor computing. Nat. Electron. 3, 664–671 (2020).
19. Yang, Y. et al. In-sensor dynamic computing for intelligent machine vision. Nat. Electron. 7, 225–233 (2024).
20. Liao, F. et al. Bioinspired in-sensor visual adaptation for accurate perception. Nat. Electron. 5, 84–91 (2022).
21. Sun, S. et al. Phase-independent wireless data aggregation via optical in-sensor computing. Nat. Commun. 17, 456 (2026).
22. Chua, L. O. Local activity is the origin of complexity. Int. J. Bifurcat. Chaos 15, 3435–3456

(2005).

23. Chua, L. O. Memristors on ‘edge of chaos’. Nat. Rev. Electr. Eng. 1, 614–627 (2024).
24. Kumar, S. & Williams, R. S. Separation of current density and electric field domains caused by nonlinear electronic instabilities. Nat. Commun. 9, 2030 (2018).
25. Frenkel, J. On pre-breakdown phenomena in insulators and electronic semi-conductors. Phys. Rev. 54, 647–648 (1938).
26. Simmons, J. G. Poole-Frenkel effect and Schottky effect in metal-insulator-metal systems. Phys. Rev. 155, 657–660 (1967).
27. Ridley, B. K. Specific negative resistance in solids. Proc. Phys. Soc. 82, 954–966 (1963).
28. Pickett, M. D., Medeiros-Ribeiro, G. & Williams, R. S. A scalable neuristor built with Mott memristors. Nat. Mater. 12, 114–117 (2013).
29. Yi, W. et al. Biological plausibility and stochasticity in scalable VO2 active memristor neurons. Nat. Commun. 9, 4661 (2018).
30. Gibson, G. A. et al. An accurate locally active memristor model for S-type negative differential resistance in NbOx. Appl. Phys. Lett. 108, 023505 (2016).
31. Kumar, S., Strachan, J. P. & Williams, R. S. Chaotic dynamics in nanoscale NbO2 Mott memristors for analogue computing. Nature 548, 318–321 (2017).
32. Kumar, S., Williams, R. S. & Wang, Z. Third-order nanocircuit elements for neuromorphic engineering. Nature 585, 518–523 (2020).
33. Binet, L. & Gourier, D. Origin of the blue luminescence of β-Ga2O3. J. Phys. Chem. Solids 59, 1241–1249 (1998).
34. Varley, J. B., Weber, J. R., Janotti, A. & Van de Walle, C. G. Oxygen vacancies and donor impurities in β-Ga2O3. Appl. Phys. Lett. 97, 142106 (2010).
35. Zacherle, T., Schmidt, P. C. & Martin, M. Ab initio calculations on the defect structure of β-Ga2O3. Phys. Rev. B 87, 235206 (2013).
36. Su, X. et al. Robust Ga2O3 memristor with sharp stable negative differential resistance for energy-efficient reliable analog resistive switching and artificial synapse applications. ACS Nano 19, 42845–42852 (2025).
37. Yeargan, J. R. & Taylor, H. L. The Poole-Frenkel effect with compensation present. J. Appl. Phys. 39, 5600–5604 (1968).
38. Lampert, M. A. Simplified theory of space-charge-limited currents in an insulator with traps. Phys. Rev. 103, 1648–1656 (1956).
39. Burkitt, A. N. A review of the integrate-and-fire neuron model: I. Homogeneous synaptic input. Biol. Cybern. 95, 1–19 (2006).
40. Tanaka, G. et al. Recent advances in physical reservoir computing: a review. Neural Netw. 115, 100–123 (2019).
41. Du, C. et al. Reservoir computing using dynamic memristors for temporal information processing. Nat. Commun. 8, 2204 (2017).
42. Moon, J. et al. Temporal data classification and forecasting using a memristor-based reservoir computing system. Nat. Electron. 2, 480–487 (2019).

Supplementary Files

This is a list of supplementary files associated with this preprint. Click to download.

- SupplementaryInformationrevised20260908.docx